J Therm Spray Tech (2021) 30:864–872
https://doi.org/10.1007/s11666-021-01172-4


PEER REVIEWED

# PS–PVD Alumina Overlayer on Thermal Barrier Coatings Against CMAS Attack

**Yiqian Guo[1,2] · Liangliang Wei[1,2] · Qing He[3] · Yangpi Deng[1] · Wenting He[1,2] · Hongbo Guo[1,2]**

Submitted: 28 September 2020 / in revised form: 30 November 2020 / Accepted: 13 December 2020 / Published online: 12 March 2021


**Abstract** Glassy deposits mainly comprising of calcium–magnesium–alumina–silicate (CMAS) accelerate the spallation of thermal barrier coatings (TBCs). In this work, an $Al_2O_3$ layer was produced on yttria-stabilized zirconia (YSZ) coating by plasma spray–physical vapor deposition (PS–PVD). The effects of processing parameters during PS–PVD process on the microstructures of the deposited $Al_2O_3$ coatings were investigated. A homogeneous $Al_2O_3$ coating with porosity less than 1% was deposited at the spray distance of 1400 mm, which is much denser than the coating produced by atmospheric plasma spray (APS) and other PS–PVD coatings sprayed at 1000 and 1900 mm. The CMAS corrosion test at 1250 °C showed that the APS $Al_2O_3$ layer was dissolved in CMAS after 24 h thermal exposure, whereas a dense reaction layer mainly composed of anorthite formed on the top region of the PS–PVD $Al_2O_3$ layer effectively protected the underlying $Al_2O_3$ layer from CMAS infiltration. Thermal cycling behavior of the PS–PVD $Al_2O_3$/YSZ TBC and the APS $Al_2O_3$/YSZ TBC at 1050 °C was compared. Bulk spallation of the APS TBC occurred within 300 h thermal cycling, while little spallation was observed on the PS–PVD TBC even after 500 h thermal cycling, indicating superior durability of the PS–PVD coating.

**Keywords** alumina · atmospheric plasma spray (APS) · calcium–magnesium–alumina–silicate (CMAS) · plasma spray–physical vapor deposition (PS–PVD) · thermal barrier coatings (TBCs) · thermal cycling

## Introduction

Thermal barrier coatings (TBCs) applied on the hot components in gas turbines provide thermal and corrosion prevention for the underlying superalloys (Ref 1-3). The ceramic topcoat in the TBC system is made of 7-8wt % yttria-stabilized zirconia (YSZ), which is usually prepared by atmospheric plasma spray (APS) or electron beam–physical vapor deposition (EB–PVD) (Ref 4-7). With the increasing service temperature of advanced gas turbines and aero-engines, the failure of YSZ TBCs caused by environmental silicate deposits mainly composed of calcium–magnesium–aluminum–silicate (CMAS) has become an urgent issue to be solved. Molten CMAS deposits penetrate the TBCs through the interconnected microcracks and porosity in the APS coating or the inter-columnar gaps in the EB–PVD coating. On the one hand, thermal–chemical interaction between CMAS and YSZ coating results in the dissolution of yttrium from YSZ, which in turn causes

This article is an invited paper selected from presentations at the 10th Asian Thermal Spray Conference (ATSC 2020) and has been expanded from the original presentation. ATSC 2020 was held in Ningbo, China, from November 1–3, 2020, and was organized by the Asian Thermal Spray Society with Ningbo Institute of Materials Technology and Engineering, Chinese Academy of Sciences as the Host Organizer

✉ Hongbo Guo
guo.hongbo@buaa.edu.cn

Liangliang Wei
weill@buaa.edu.cn

[1] School of Materials Science and Engineering, Beihang University, No. 37 Xueyuan Road, Beijing 100191, China

[2] Key Laboratory of High-Temperature Structural Materials and Protective Coatings (Ministry of Industry and Information Technology), Beihang University, No. 37 Xueyuan Road, Beijing 100191, China

[3] Surface Engineering Research Institute, Chinese Academy of Agricultural Mechanization Sciences, Beijing 100083, China

tetragonal–monoclinic phase transformation of $ZrO_2$ accompanied with volume expansion. On the other hand, CMAS penetration accelerates sintering and stiffening of YSZ coating, leading to a reduction in porosity and loss of strain tolerance (Ref 8-10).

So far, many approaches have been attempted to mitigate CMAS penetration at high temperature for YSZ TBCs. One of the approaches is physical insulation by depositing a chemically inert film made of noble metals such as Pd or Pt which doesn't react with molten CMAS to arrest CMAS infiltration (Ref 11-14). However, its application was limited by the expensive cost, insufficient binding with the underlying TBC as well as restricted operating temperature. Another approach is chemical protection through preparing a sacrificial layer that could positively interact with CMAS glass to generate a dense and stable reaction layer for CMAS prevention (Ref 15). Or some Ti and Al were doped in the YSZ coating, which (Ref 16, 17) promotes the crystallization of CMAS glass and the formation of reaction layer, thus effectively against further CMAS attack before infiltration.

Alumina is recognized as a promising candidate for resisting CMAS attack because of its ability to shift the composition of molten CMAS to a field where glasses are easy to crystallize (Ref 18-20). Besides, $Al_2O_3$ modified YSZ TBCs are demonstrated to have enhanced mechanical properties (Ref 21). Accordingly, the $Al_2O_3$ coatings have been intensively used to prevent CMAS attack. Zhang et al. (Ref 19) have obtained an in-situ $Al_2O_3$ layer by magnetron sputtering Al film on YSZ and vacuum heat treatment. Mohan et al. (Ref 20) have prepared an $Al_2O_3$ film by electrophoretic deposition followed by sintering at 1200 °C. Nevertheless, sintering treatment is detrimental to the mechanical properties of the coating. Furthermore, the column gaps in the $Al_2O_3$ coatings deposited by PVD provide an open pathway for the infiltration of glassy CMAS deposits (Ref 21-23). The $Al_2O_3$ coatings prepared by APS possess internal defects, interconnected microcracks, and high porosity, which are also not effective in blocking CMAS penetration. Besides, premature spallation of the APS $Al_2O_3$ overlayer on the YSZ TBC system occurs due to the poor thermal cycling durability (Ref 24, 25).

A dense protective layer is essential in order to prevent molten CMAS infiltration. In the present work, $Al_2O_3$ coatings were produced by plasma spray–physical vapor deposition (PS–PVD). For this application, at an intermediate electric net power of approximately 40 kW, the vaporization degree of the feedstock can be limited, and mainly liquid phase deposition is obtained (Ref 26, 27). In this way, a thin and dense protective $Al_2O_3$ overlayer for the YSZ TBCs against CMAS attack can be produced. The influences of processing parameters on the microstructures of the sprayed $Al_2O_3$ coatings were investigated. The resistance to CMAS corrosion and thermal cycling behavior of the PS–PVD $Al_2O_3$ overlayer/YSZ TBC system and APS $Al_2O_3$ overlayer/YSZ TBC system were studied comparatively and the associated mechanisms were discussed.

## Materials and Methods

### Preparation of TBCs

Nickel-based superalloy K403 was chosen as the substrate materials, which were cut into disk shape samples of 20 mm in diameter and 3 mm in thickness. The feedstock materials were commercial 8YSZ powder (METCO 204 NS) and Ni-21Co-17Cr-12Al-1Y (Ni 192-8) powder for the YSZ topcoat and metallic bond coat, respectively. The YSZ topcoat approx. 200 μm thick and the NiCoCrAlY bond coat approx. 150 μm thick were both prepared using an APS unit (Sulzer Metco) with a 9M gun.

The powder feedstock for the $Al_2O_3$ overlayer was prepared by spray drying, which was micrometer agglomerated, as shown in Fig. 1, with a size distribution: $d_{10}$ = 20 μm, $d_{50}$ = 27 μm and $d_{90}$ = 37 μm. The $Al_2O_3$ overlayer was deposited by PS–PVD (Medicoat AG, Switzerland) with an MC-100 plasma torch, which allowed a maximum current of 2500 A and a peak power of 150 kW. The spray parameters for $Al_2O_3$ coatings are shown in Table 1, in which three spray distances of 1000 mm, 1400 mm, and 1900 mm were used for obtaining dense coating. For comparison, an $Al_2O_3$ overlayer with similar thickness was also prepared by APS with the processing parameters as shown in Table 2.

### CMAS Preparation and Corrosion Test

CMAS powders with a chemical composition of 31CaO–8MgO–12$Al_2O_3$–49$SiO_2$ were prepared for the following corrosion test to simulate the environmental deposits in an aero-engine service environment. The preparation of the CMAS powders was described elsewhere (Ref 28).

Before the corrosion test, the ball-milled CMAS powder was dissolved in ethanol and deposited homogeneously onto the surfaces of the TBC specimens, then dried and weighed to maintain a deposit concentration of 15 mg/cm$^2$. The TBC specimens with CMAS deposits were calcined in an air furnace at 1250 °C for 24 h to exam the corrosion resistance of the $Al_2O_3$ overlayers.

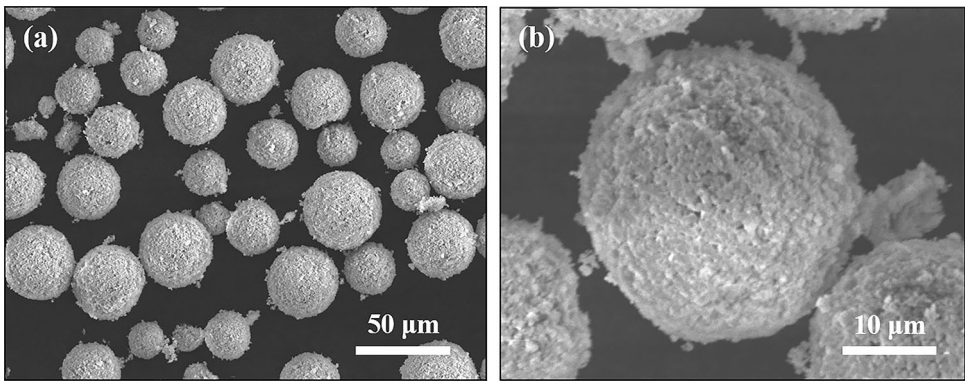


**Fig. 1.** Surface morphologies of feedstock powder for spraying $Al_2O_3$ coatings: (a) lower magnification and (b) higher magnification.

**Table 1** PS–PVD processing parameters for spraying $Al_2O_3$ coatings

| | |
|---|---|
| Plasma gas | Ar 30 slpm/He 60 slpm |
| Net power | 40 kW |
| Powder feed rate | 5 g/min |
| Carrier gas | Ar 3 slpm |
| Pressure | 10 mbar |
| Spray distance | 1000, 1400, 1900 mm |
| Substrate temperature | 900–1000 °C |

*Slpm* standard liters per minute

**Table 2** APS processing parameters for spraying $Al_2O_3$ coating

| Parameters | $Al_2O_3$ coating |
|---|---|
| Power | 63 kW |
| Plasma gas | Ar 86 slpm/$H_2$ 60 slpm |
| Spray distance | 110 mm |
| Powder feeding | 13–18 g/min |

### Thermal Cycling Tests

The thermal cycling test was carried out in an air tube furnace with a mechanical automation system. During the testing, the TBC-coated specimens were first heated in the furnace at 1050 °C for 50 min, then followed by 10 min compressive air cooling from both sides of the specimen. The surface condition of the coated specimens was examined after every 10 cycles.

### Characterization

The surface and cross-sectional morphologies of as-sprayed TBCs and CMAS-interacted TBCs were characterized by a Field Emission-Scanning Electron Microscope (FE-SEM, Apollo 300) equipped with the energy dispersive X-ray spectrometry (EDS) and backscattered electron (BSE) detector. The phase constituents of the coatings before and after interaction with CMAS were determined by X-ray diffraction (XRD, Rigaku D/max2200PC) using Cu-Kα radiation with a step size of 6°/min and scanning angle from 20° to 80°.

## Results and Discussion

### Microstructures of the As-Sprayed $Al_2O_3$ Coatings

Figure 2(a), (c), and (d) shows the surface morphologies of the as-sprayed coatings deposited at 1000, 1500, and 1900 mm, respectively. All the sprayed coatings mainly consist of splats, resulting from impingement, spreading, and subsequent solidification of liquid droplets. Besides, there are some sintered nano-sized particles as seen in the high magnification SEM micrograph (Fig. 2b), which are probably from un-melted or partially melted primary particles in the feedstock powder. Note that the coating sprayed at 1000 mm exhibits more nanoparticles as compared to the coatings sprayed at 1400 and 1900 mm.

The porosity measurement was taken on polished cross sections of the $Al_2O_3$ coatings based on image analyses, and the corresponding results are given in Table 3. The maximum porosity is only 2.6% which belongs to the coating sprayed at 1000 mm. The lowest porosity of $\sim$ 0.8% was achieved in the coating sprayed at 1400 mm. From these results, the $Al_2O_3$ overlayers by PS–PVD are quite dense, which means that the coatings were deposited mainly from well-melted liquid droplets.

Figure 3(a), (b), and (c) shows the fracture morphologies of PS–PVD $Al_2O_3$ coatings deposited at 1000, 1400, and 1900 mm, respectively. The coatings reveal a different thickness although the coatings were sprayed within the same duration. In particular, the coating sprayed at 1000 mm is nearly twice as thick as the other two coatings sprayed at longer distances and falls off the substrate after coating process as shown in Fig. 3(a).

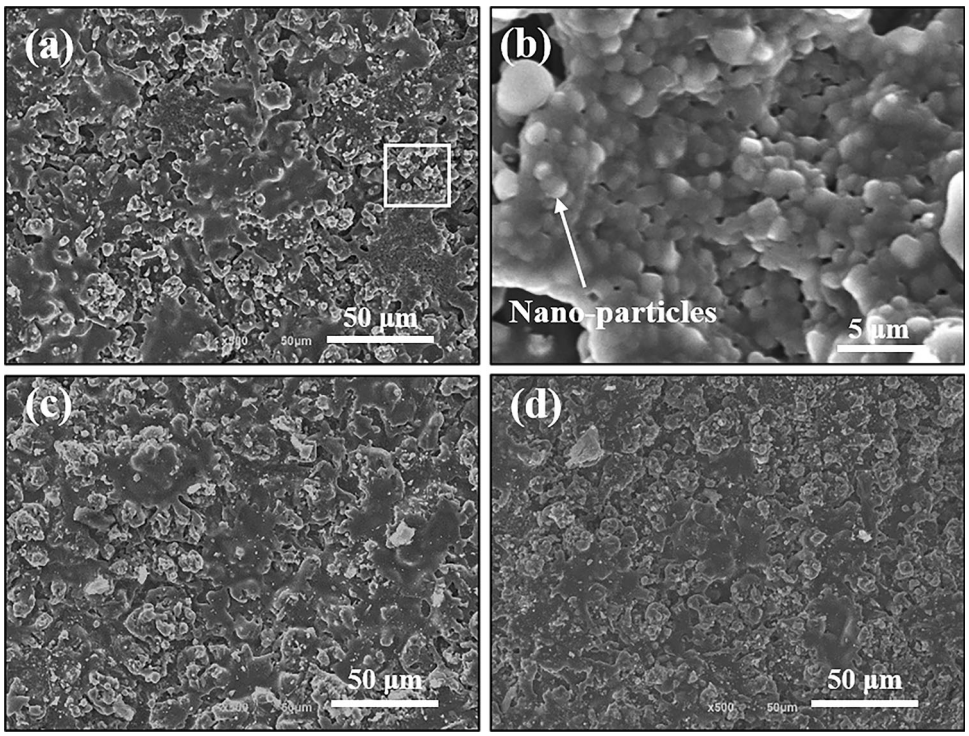


**Fig. 2.** Surface morphologies of PS–PVD $Al_2O_3$ coatings deposited at different distances: (a) 1000 mm, (b) higher magnification of the area selected in (a, c) 1400 mm, and (d) 1900 mm

**Table 3** Porosities of PS–PVD $Al_2O_3$ coatings

| Spray distance (mm) | 1000 | 1400 | 1900 |
|---|---|---|---|
| Porosity (%) | 2.61 ± 0.05 | 0.82 ± 0.02 | 1.53 ± 0.03 |

Compared to typical PS–PVD conditions for columnar coatings deposition, the plasma jet under the conditions in this paper is more concentrated due to higher chamber pressure 1000 Pa. As spraying distance increases, the heating effects of the plasma jet on powder feedstock become weaker, and the velocity of particles decreases. Based on this analysis, one possible reason for thinner coatings at long spraying distances could be some large particles were out of the deposition area due to reduced velocity and gravity. Accordingly, the porosity of the coating sprayed at 1400 mm is smaller than that of the coating sprayed at 1000 mm due to less un-melted particle deposition. However, with further increasing the spray distance to 1900 mm, solidification of liquid droplets in the plasma jet was likely occurred because of insufficient heat transfer from the plasma jet. This could result in a slightly increased porosity due to the deposition of solidified particles. Furthermore, a low substrate temperature at long spray distance due to less heat transfer from the plasma jet is not conducive to droplet deposition, which may be also responsible for the low deposition rates at long distances.

As the porosity is an important criterion for evaluating the capability of a coating resistant to CMAS corrosion and infiltration, the coating sprayed at 1400 mm was considered as the optimized microstructure for CMAS protection in this paper.

Figure 4(a) shows the cross-sectional micrographs of the PS–PVD $Al_2O_3$ overlayer deposited at the spray distance of 1400 mm and a reference APS $Al_2O_3$ overlayer. By optimized processing parameters for APS (listed in Table 2), the porosity (6.5%) of APS $Al_2O_3$ coating is still higher than that of the PS–PVD $Al_2O_3$ (only 0.82%).

## CMAS Corrosion Tests

CMAS infiltration tests were performed on both $Al_2O_3$ coating and 8YSZ coating in order to compare the corrosion resistance of the two TBCs. After 24 h testing, many cracks and spallation were visible on the surface of YSZ coatings, as seen in Fig. 5(a), which led to surface wrinkle and coating spallation. The cross-sectional micrograph of YSZ TBC is shown in Fig. 5(b). The structure of the upper zone of YSZ coating is quite loose with obvious small globular particles which indicates dissolution and corrosion of YSZ by the molten CMAS. The EDS line scanning (Fig. 5c and d) showing the concentration of Si and Ca along the arrow direction in Fig. 5(b) demonstrates that the minimum infiltration depth of molten CMAS for YSZ coating was at least 50 μm.

Similarly, the bilayer $Al_2O_3$/YSZ TBCs were calcined with CMAS glass under same isothermal treatment conditions to compare the infiltration resistance of APS $Al_2O_3$ and PS–PVD $Al_2O_3$ coatings. The cross-sectional morphologies of the bilayer $Al_2O_3$/YSZ coatings after interaction with molten CMAS are shown in Fig. 6. As for APS $Al_2O_3$/YSZ coatings (Fig. 6a), the CMAS infiltration depth evidenced by the Si detection was about 50 µm (Fig. 6e). What's more, those loose and small particles at the $Al_2O_3$/YSZ interface indicate the underlying YSZ also slightly reacted with CMAS. From the cross-sectional morphology in Fig. 6(b), CMAS has infiltrated through the pores into the interior coating and reacted with YSZ at the interface. This means that APS $Al_2O_3$ coating offers weak resistance to CMAS corrosion.

Figure 6(c) shows the cross-sectional SEM image of PS–PVD $Al_2O_3$/YSZ coatings after interaction with CMAS at 1250 °C for 24 h, where the respective elemental distributions of Ca and Si are given in Fig. 6(f) and (g). Note that Ca and Si content decreased dramatically at the detection depth of about 10 µm, indicating that the infiltration of CMAS glass was successfully resisted by PS–PVD $Al_2O_3$ overlay. Figure 6(d) shows the dense reaction layer on top of PS–PVD $Al_2O_3$/YSZ coatings and corresponding Ca, Mg, Al, and Si elemental content at points 1 to 6 is summarized in Table 4. The presence of Ca, Mg, Al, and Si elements is detected at point 1 to point 4, particularly, the content of Ca and Si reduces gradually through the coating thickness, which indicates that a dense 4 µm thick reaction layer generated during the period of CMAS corrosion. At point 6, a depth of around 10 µm, the $Al_2O_3$ layer is intact

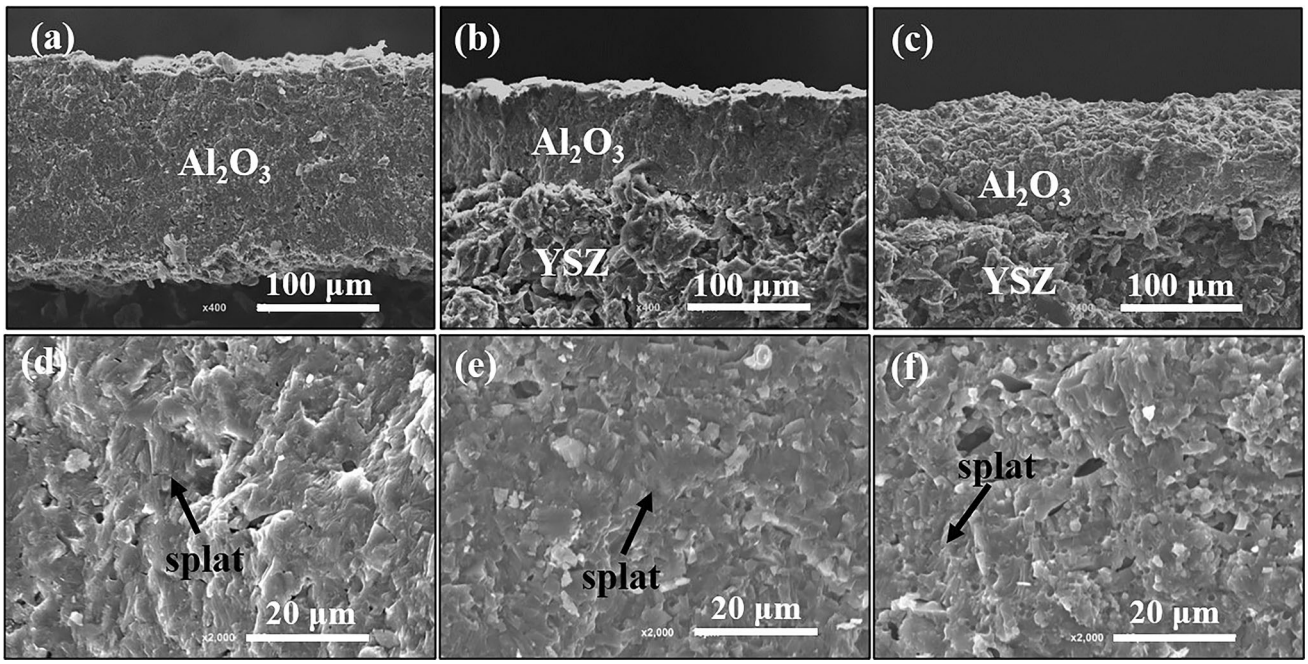


**Fig. 3.** Fracture morphologies of cross sections of PS–PVD $Al_2O_3$ coatings deposited at different distances: (a) 1000 mm, (b) 1400 mm, (c) 1900 mm, and (d, e, f are magnifications of (a, b, and c), respectively

**Fig. 4.** SEM micrographs of cross sections of $Al_2O_3$ coatings prepared by PS–PVD at 1400 mm (a) and by APS (b)

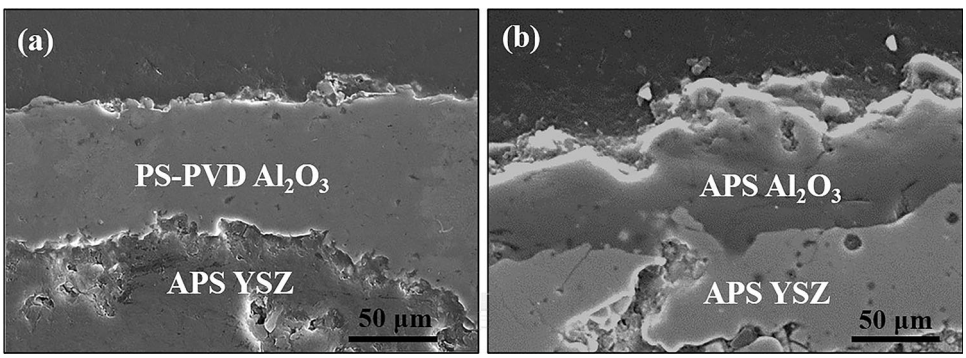

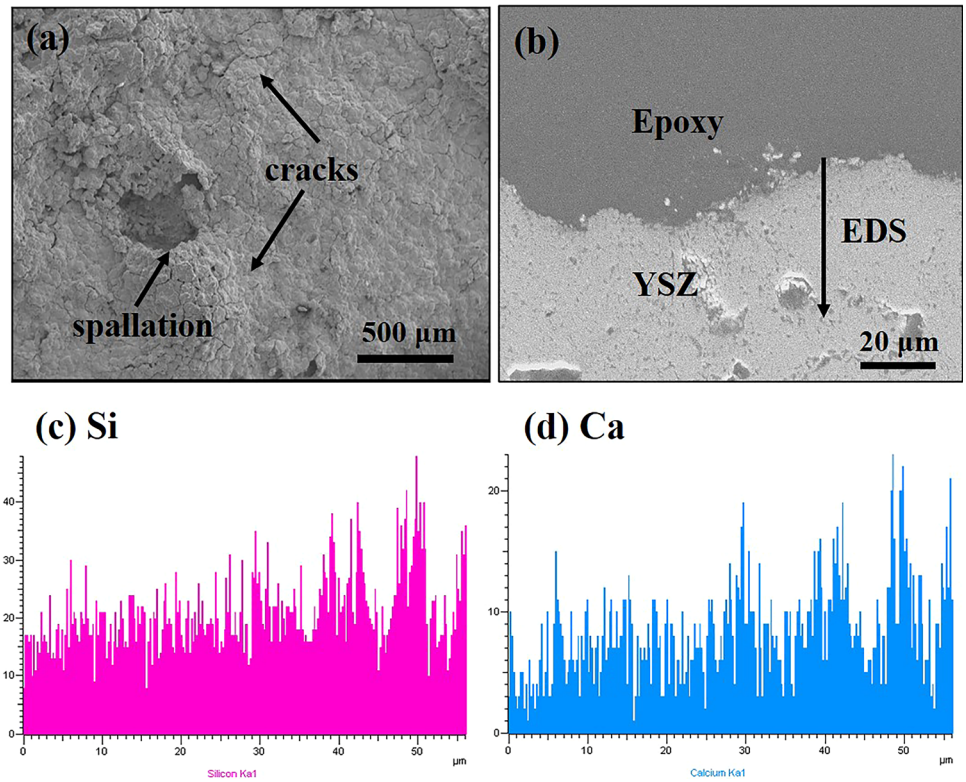


**Fig. 5.** SEM morphologies of the surface (a) and cross section (b) of the YSZ coating after CMAS corrosion at 1250 °C for 24 h, and element distribution of Ca (c) and Si (d) across the coating thickness toward the arrow direction in (b)

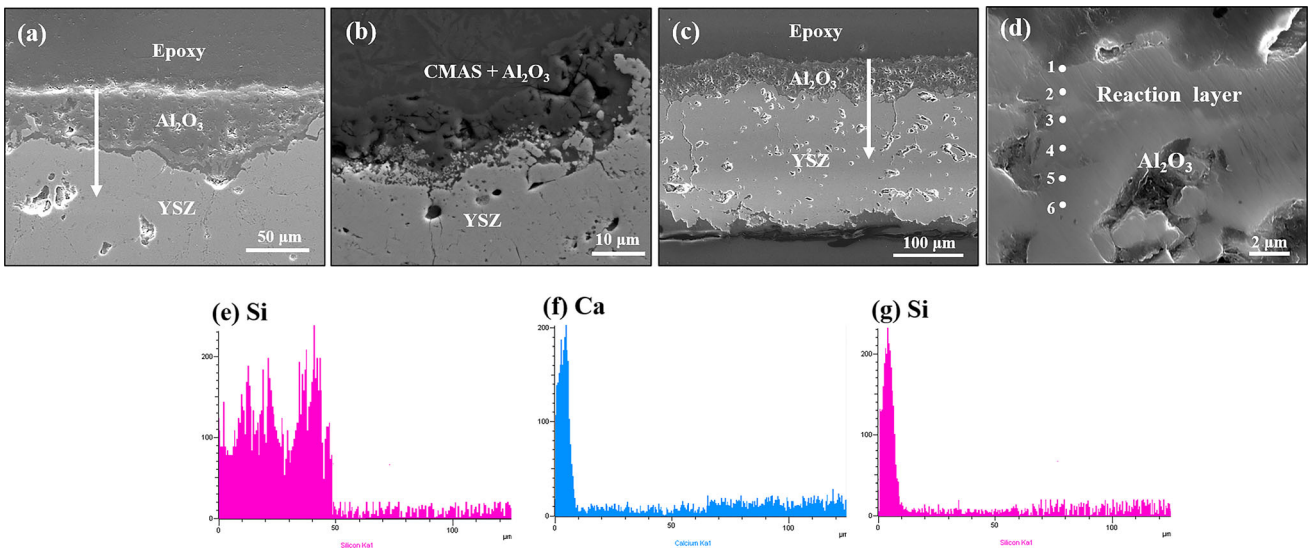


**Fig. 6.** Cross-sectional micrographs of coatings after CMAS corrosion at 1250 °C for 24 h. (a) APS $Al_2O_3$/YSZ coating, (b) magnification at the interface of APS $Al_2O_3$/YSZ, (c) PS–PVD $Al_2O_3$/YSZ coating, (d) magnification of the top area in (c, e) Si distribution along the arrow direction in (a), and (f) Ca and (g) Si distribution along the arrow direction in (c)

and CMAS components can hardly be found. In addition, this result also indicates that in order to obtain a better protection the thickness of $Al_2O_3$ coating must be at least 10 µm.

Figure 7(a) and (b) shows the surface morphologies of the PS–PVD alumina overlayer with bare holes and cracks. The chemical composition of the region marked by the red rectangle in Fig. 7(b) is identified by EDS and listed in Table 5. The composition with atom ratio of Ca (12.35 at.%), Al (22.38 at.%), and Si (24.20 at.%) close to 1:2:2 is deviated from the original CMAS composition. To identify the reaction products, XRD analyses are performed on as-sprayed $Al_2O_3$ coating and the one after CMAS corrosion (Fig. 8). According to the phase structural

analyses, the original PS–PVD $Al_2O_3$/YSZ coating is composed of α-$Al_2O_3$ and $ZrO_2$. After 24 h interaction with CMAS, the peaks of anorthite and spinel could be detected. Combined with the EDS results in Table 5, the composition of anorthite could be $CaAl_2Si_2O_8$. Anorthite and spinel were demonstrated to start to melt at temperature above 1550 °C, which is much higher than CMAS melting point and operating temperature of TBCs (1250 °C in this paper) (Ref 16, 29, 30). Thus, these high melting point reaction products can inhibit the infiltration of molten CMAS on one hand. On the other hand, compared with APS $Al_2O_3$ coating, the PS–PVD $Al_2O_3$ coating possesses higher density which did not provide infiltration paths to molten CMAS before formation of stable high melting point production. These should be reasons for the better CMAS resistance of the PS–PVD $Al_2O_3$ overlayer at 1250 °C.

### *Thermal Cycling Behavior of PS–PVD $Al_2O_3$/YSZ Coating System*

Considering the potential spallation of an in-service environment induced by mismatch coefficients of thermal expansion (CTE) between $Al_2O_3$ and YSZ, thermal cycling of bilayer PS–PVD $Al_2O_3$/YSZ TBCs was studied. Figure 9 shows the surface photographs of the as-sprayed $Al_2O_3$/YSZ coating cycled 100 and 500 h at 1050 °C, respectively. It can be seen that the coating surface kept almost intact except for a little spallation at the sample edge even though the surface changed to blue color due to oxidation, which implies an excellent lifetime of more than 500 h for PS–PVD $Al_2O_3$/YSZ TBCs. The surface morphologies of the as-sprayed $Al_2O_3$/YSZ and after 100, 500 h thermal cycling tests are shown in Fig. 10. The white small spots in Fig. 10(b) and (c) implied that the YSZ coating was already exposed attributed to the spallation of the $Al_2O_3$ overlayer. But it is good that the spallation area

**Table 4.** Chemical compositions of dots 1-6 in Fig. 6d

| Element (at. %) | Ca | Al | Si | Mg | O |
|---|---|---|---|---|---|
| 1 | 12.35 | 22.28 | 24.20 | 0.36 | Bal. |
| 2 | 8.73 | 27.72 | 19.63 | 0.69 | Bal. |
| 3 | 2.54 | 46.77 | 6.18 | 0.47 | Bal. |
| 4 | 1.24 | 64.56 | 2.10 | 0.67 | Bal. |
| 5 | … | 53.03 | 1.84 | … | Bal. |
| 6 | … | 42.83 | … | … | Bal. |

**Table 5.** Chemical compositions of the region enclosed by the red rectangle in Fig. 7(b)

| Element | Ca | Al | Si | Mg | O |
|---|---|---|---|---|---|
| at.% | 12.35 | 22.28 | 24.20 | 0.36 | Bal |

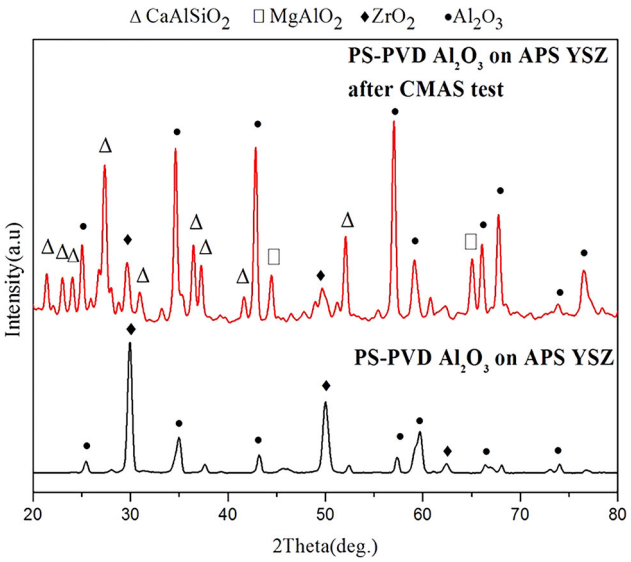


**Fig. 8.** XRD patterns of (a) as-sprayed $Al_2O_3$/YSZ coating and (b) the coating with CMAS deposit after 24 h exposure at 1250 °C

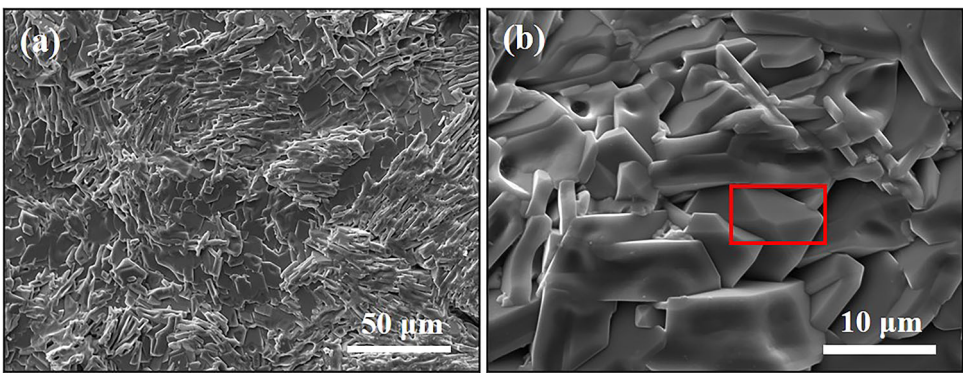


**Fig. 7.** Surface morphologies of PS–PVD $Al_2O_3$/YSZ coatings after CMAS corrosion at 1250 °C for 24 h: (a) at lower magnification and (b) at higher magnification

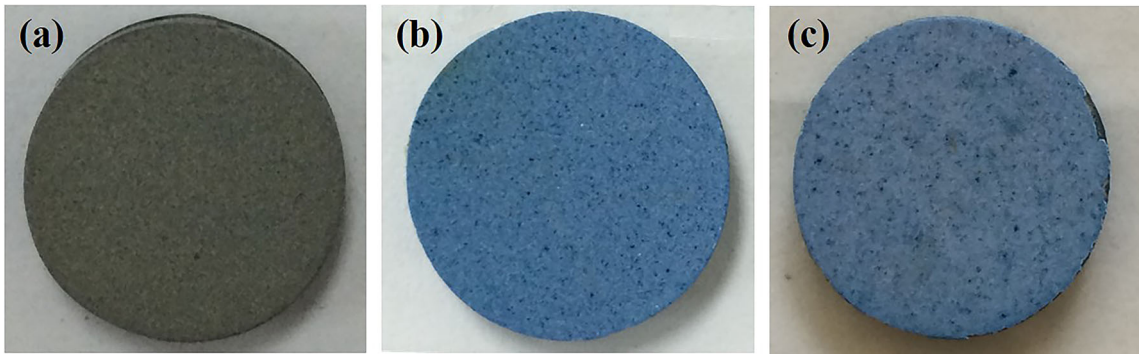


**Fig. 9.** Photographs of surfaces of as-sprayed PS–PVD $Al_2O_3$/YSZ coating sample (a) and the coating sample thermal cycled at 1050 °C for 100 h (b) and 500 h (c)

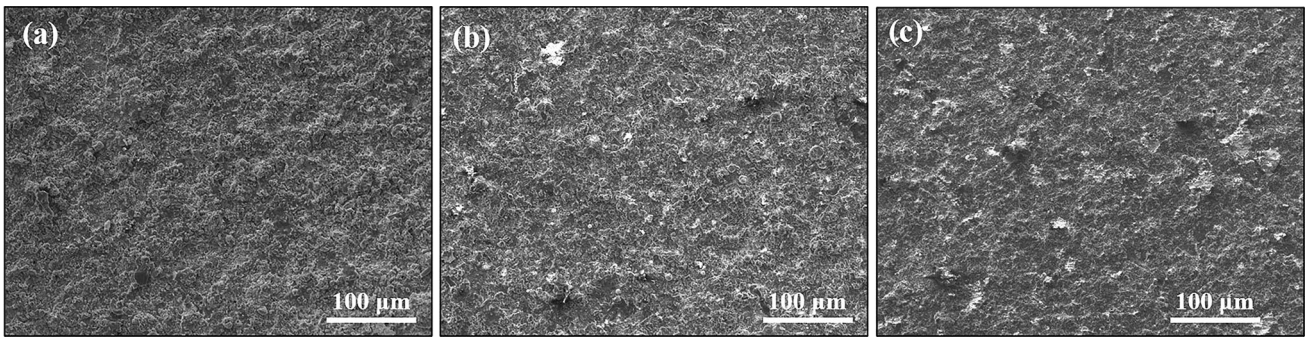


**Fig. 10.** Surface morphologies of as-sprayed PS–PVD $Al_2O_3$/YSZ coating sample (a) and the coating thermal cycled at 1050 °C for 100 h (b) and 500 h (c)

is no more than 2% of the whole surface after 500 h thermal cycling.

As a control, the thermal cycling test was also conducted for APS $Al_2O_3$/YSZ TBCs, whose failure occurred as soon as the thermal cycling time reached 300 h. This comparison shows that PS–PVD $Al_2O_3$/YSZ TBCs owns better thermal cycling durability than APS $Al_2O_3$/YSZ TBCs. A possible reason could be the better bonding strength between PS–PVD $Al_2O_3$ and YSZ coating due to the high substrate temperature and well-melted $Al_2O_3$ droplets.

## Conclusions

A thin and dense $Al_2O_3$ overlayer was deposited by PS–PVD on YSZ TBC. Its resistance to CMAS interaction and thermal cycling behavior were investigated. Some conclusions can be drawn as follows:

1. The PS–PVD $Al_2O_3$ overlayers PS–PVD are mainly deposited from well-melted droplets They possess much lower porosity (optimal 0.82% deposited at the spray distance of 1400 mm) than that of APS $Al_2O_3$ overlayer.
2. The thin and dense PS–PVD $Al_2O_3$/YSZ TBCs exhibit excellent CMAS resistance because of low porosity and formation of dense reaction layer composed of anorthite and spinel preventing the penetration of molten CMAS.
3. The PS–PVD-$Al_2O_3$-coated specimens show a good thermal cycling lifetime more than 500 h, about 65% longer than that of APS-$Al_2O_3$-coated specimens (300 h).

In summary, the $Al_2O_3$ overlayer deposited on APS YSZ coating by PS–PVD exhibits excellent CMAS resistance and thermal cycling durability. The PS–PVD $Al_2O_3$ overlayer can be regarded as one of the promising protective coatings for YSZ TBCs.

**Acknowledgments** This research is sponsored by National Key Technologies R&D Program of China under Grant No. 2017YFB0306103, National Science and Technology Major Project under Grant No. 2017-VI-0010-0081, Nature Science Foundations of China (NFSC) under Grant No. 51590894 and 51901107, and the 111 Project (B17002).

## References


1. E. Bakan and R. Vasen, Ceramic Top Coats of Plasma-Sprayed Thermal Barrier Coatings: Materials, Processes, and Properties, *J. sTherm. Spray. Technol.*, 2017, **26**, p 992–1010.
2. R.A. Miller, Current Status of Thermal Barrier Coatings—An Overview, *Surf. Coat. Technol.*, 1987, **30**, p 1–11.
3. J. Wang, X. Yu, C. Rong and Z.J. Feng, Microstructure and Thermal Properties of $RETaO_4$ (RE = Nd, Eu, Gd, Dy, Er, Yb, Lu) as Promising Thermal Barrier Coating Materials, *Scr. Mater.*, 2017, **126**, p 24–28.
4. N.P. Padture, M. Gell and E.H. Jordan, Thermal Barrier Coatings for Gas-Turbine Engine Applications, *Science*, 2002, **296**, p 280–284.
5. R. Vaßen, M.O. Jarligo and T. Steinke, Overview on Advanced Thermal Barrier Coatings, *Surf. Coat. Technol.*, 2010, **205**, p 938–942.
6. D.F. Zambranoad, A. Barrios, L.E. Tobon, C. Serna, P. Gomeza, J.D. Osorioc and A. Toro, Thermal Properties and Phase Stability of Yttria-Stabilized Zirconia (YSZ) Coating Deposited by Air Plasma Spray on to a Ni-Base Superalloy, *Ceram. Int.*, 2018, **44**, p 3625–3635.
7. S. Uwe, S. Bilge, F. Klaus and L. Christoph, Review on Advanced EB-PVD Ceramic Topcoats for TBC Applications, *Int. J. Appl. Ceram. Technol.*, 2004, **1**, p 302–315.
8. T.R. Kakuda, C.G. Levi and T.D. Bennett, The Thermal Behavior of CMAS-Infiltrated Thermal Barrier Coatings, *Surf. Coat. Technol.*, 2015, **272**, p 350–356.
9. A.R. Krause, X. Li and N.P. Padture, Interaction Between Ceramic Powder and Molten Calcia–Magnesia–Alumina–Silicate (CMAS) Glass and Its Implication on CMAS-Resistant Thermal Barrier Coatings, *Scr. Mater.*, 2016, **112**, p 118–122.
10. A.R. Krause, H.F. Garces and G. Dwivedi, Calcium–Magnesia–Alumina–Silicate (CMAS)-Induced Degradation and Failure of Air Plasma Sprayed Yttria-Stabilized Zirconia Thermal Barrier Coatings, *Acta Mater.*, 2016, **105**, p 355–366.
11. S. Krämer, S. Faulhaber and M. Chambers, Mechanisms of Cracking and Delamination Within Thick Thermal Barrier Systems in Aero-Engines Subject to Calcium–Magnesium–Alumina–Silicate (CMAS) Penetration, *Mater. Sci. Eng. A*, 2008, **490**, p 26–35.
12. C. Mercer, S. Faulhaber and A.G. Evans, A Delamination Mechanism for Thermal Barrier Coatings Subject to Calcium–Magnesium–Alumina–Silicate (CMAS) Infiltration, *Acta Mater.*, 2005, **53**, p 1029–1039.
13. L. Wang, L. Guo and Z. Li, Protectiveness of Pt and $Gd_2Zr_2O_7$, Layers on EB-PVD YSZ Thermal Barrier Coatings Against Calcium–Magnesium–Alumina–Silicate (CMAS) Attack, *Ceram. Int.*, 2015, **41**, p 11662–11669.
14. A.K. Rai, R.S. Bhattacharya and D.E. Wolfe, CMAS-Resistant Thermal Barrier Coatings (TBC), *Inter. J. Appl. Ceram. Technol.*, 2010, **7**, p 662–674.
15. S. Uwe and B. Wolfgang, Degradation of $La_2Zr_2O_7$ and Other Novel EB-PVD Thermal Barrier Coatings by CMAS (CaO–$MgO$–$Al_2O_3$–$SiO_2$) and Volcanic Ash Deposits, *Surf. Coat. Technol.*, 2013, **235**, p 165–173.
16. A. Aygun, A.L. Vasiliev and N.P. Padture, Novel Thermal Barrier Coatings that are Resistant to High-Temperature Attack by Glassy Deposits, *Acta Mater.*, 2007, **55**, p 6734–6375.
17. J.M. Drexler, K. Shinoda and A.L. Ortiz, Air-Plasma-Sprayed Thermal Barrier Coatings that are Resistant to High-Temperature Attack by Glassy Deposits, *Acta Mater.*, 2010, **58**, p 6835–6844.
18. X.Q. Cao, R. Vassen and D. Stoever, Ceramic Materials for Thermal Barrier Coatings, *J. Eur. Ceram. Soc.*, 2004, **24**, p 1–10.
19. X.F. Zhang, K.S. Zhou and X. Wei, In Situ Synthesis of α-Alumina Layer on Thermal Barrier Coating for Protection Against CMAS (CaO–$MgO$–$Al_2O_3$–$SiO_2$) Corrosion, *Surf. Coat. Technol.*, 2015, **261**, p 54–59.
20. P. Mohan, B. Yao and T. Patterson, Electrophoretically Deposited Alumina as Protective Overlay for Thermal Barrier Coatings Against CMAS Degradation, *Surf. Coat. Technol.*, 2009, **204**, p 797–801.
21. B. Yin, F. Zhang, W. Zhu, L. Yang and Y. Zhou, Effect of $Al_2O_3$ Modification on the Properties of YSZ: Corrosion Resistant, Wetting and Thermal-Mechanical Properties, *Surf. Coat. Technol.*, 2019, **357**, p 161–171.
22. R. Naraparaju, R.P. Pubbysetty, P. Mechnich and S. Uwe, EB-PVD Alumina ($Al_2O_3$) as a Top Coat on 7YSZ TBCs Against CMAS/VA Infiltration: Deposition and Reaction Mechanisms, *J. Eur. Ceram. Soc.*, 2018, **38**, p 3333–3346.
23. H. Peng, L. Wang and L. Guo, Degradation of EB-PVD Thermal Barrier Coatings Caused by CMAS Deposits, *Progr. Nat. Sci Mater. Int.*, 2012, **22**, p 461–467.
24. F. Goutier, S. Valette and M. Vardelle, Alumina Plasma Spraying on 304L Stainless Steel: Role of a Wüstite Interlayer, *J. Eur. Ceram. Soc.*, 2011, **31**, p 1685–1694.
25. D.G. Girolamo, A. Brentari and C. Blasi, Microstructure and Mechanical Properties of Plasma Sprayed Alumina-Based Coatings, *Ceram. Inter.*, 2014, **40**, p 12861–12867.
26. J. Xiao, Q. Guo, L.L. Wei, W.T. He and H.B. Guo, Microstructures and Phases of Ytterbium Silicate Coatings Prepared by Plasma Spray-Physical Vapor Deposition, *Materials*, 2020, **13**, p 1721.
27. D. Marcano, G. Mauer, R. Vaßen and A. Weber, Manufacturing of High Performance Solid Oxide Fuel Cells (SOFCs) with Atmospheric Plasma Spraying (APS) and Plasma Spray-Physical Vapor Deposition (PS-PVD), *Surf. Coat. Technol.*, 2017, **318**, p 170–177.
28. L. Wang, L. Guo, Z. Li, H. Peng, Y. Ma, S.K. Gong and H.B. Guo, Protectiveness of Pt and $Gd_2Zr_2O_7$ layers on EB-PVD YSZ thermal Barrier Coatings Against Calcium–Magnesium–Alumina–Silicate (CMAS) Attack, *Ceram. Int.*, 2015, **41**, p 11662–11669.
29. A. Aygun, *Novel Thermal Barrier Coatings (TBCs) That Are Resistant to High Temperature Attack by CaO–MgO–Al2O3–SiO2 (CMAS) Glassy Deposits (CMAS) Glassy Deposits*, The Ohio State University, Ohio, 2008.
30. V.L. Wiesner and N.P. Bansal, Mechanical and thermal properties of calcium-magnesium-alumino-silicate (CMAS) glass, *J. Eur. Ceram. Soc.*, 2015, **35**, p 2907–2914.